Single-sized phase-change metasurfaces for dynamic information multiplexing and encryption

Tingting Liu [1,2] Jie Li [3] and Shuyuan Xiao [1,2,*]

[1] *School of Information Engineering, Nanchang University, Nanchang 330031, China*

[2] *Institute for Advanced Study, Nanchang University, Nanchang 330031, China*

[3] *Optoelectronic Sensor Devices and Systems Key Laboratory of Sichuan Provincial University, College of Optoelectronic Engineering, Chengdu University of Information Technology, Chengdu 610225, China*

(Received 28 January 2024; accepted 18 May 2024; published 7 June 2024)

Optical metasurfaces empower us to manipulate the electromagnetic space and control light propagation at the nanoscale, offering a powerful tool to achieve modulation of light for information processing and storage. In this paper, we propose a phase-change metasurface to realize dynamic multiplexing and encryption of near-field information. Based on the orientation degeneracy and polarization control governed by Malus's law, we elaborately design the orientation distribution of Sb_2S_3 meta-atoms with the same dimension to simultaneously satisfy the amplitude modulation requirements of three independent channels. Using the corresponding polarization control as decoding keys, three different nanoprinting images can be displayed, and these multiplexed images can be switched on and off by leveraging the reversible tunability of the Sb_2S_3 meta-atoms between the amorphous and crystalline states. With the unparalleled advantages of ultracompactness, simple design strategy, high information density and security, the proposed metasurfaces afford promising prospects for high-end applications in ultracompact and intelligent dynamic display, high-dense optical data storage, and optical information encryption.

DOI: 10.1103/PhysRevResearch.6.023258

I. INTRODUCTION

The ability to modulate light on demand is the key to modern photonic systems. Recent decade has witnessed remarkable progress in metasurfaces, which enable optical elements with potential size, weight, power, and cost benefits, especially the flexibility to tailor intrinsic properties of incident light such as amplitude, phase, and polarization at the subwavelength [1–5]. By carefully designing planar nanostructures with spatially varying field distributions across the surface, metasurfaces have led the way to meta-optics for many optical elements with various functionalities such as beam steering [6,7], focusing [8–14], spin Hall effect [15–19], holographic [20–24] and nanoprinting [25–28] imaging. Benefiting from the design flexibility, metasurfaces-based devices are evolving from single to multiple functionalities, exhibiting significant potential in information storage and encryption. Previous researches have reported different design approaches such as segmenting [29,30], layer stacking [31–35], and interleaving [36–40], for multichannel image displaying and information encoding. Yet, most of them are essentially the simple hybrids of several single-functional devices, since the operational zones of metasurfaces are divided into several segments corresponding to different functionalities. In order to further enhance information density and security, single-cell metasurfaces by taking full advantages of the design degrees of freedom of a single nanostructure are widely explored [41–43]. Nevertheless, the integration of multifold information usually requires many nanostructures with different dimensions patterned in a single piece, inevitably increasing the fabrication difficulty. Very recently, information multiplexing based on single-sized metasurfaces has also been reported through modulation across multiple optical properties [44,45]. However, most of these previous studies usually consider the far-field holographic imaging, and the quest for capability limit of the near-field information in a single-sized metasurface has been rarely explored. Therefore, there is a strong need to develop a simple design strategy of near-field nanoprinting imaging using single-sized metasurfaces enabling high level of integration and miniaturization in date storage and encryption.

Most recently, metasurfaces are in the revolutionary process from passive to active tunability towards intelligent integrated photonic devices. The reconfigurable metasurface with dynamical optical responses is highly desirable in realizing agilely switchable and reconfigurable photonic functionalities, allowing new opportunities for tailoring the light propagation and interaction with matter. Because the optical response of metasurface usually relies on the dimensions and dielectric properties, substantial efforts have explored the tuning mechanisms of integrating tunable materials into nanostructures. By leveraging external stimuli such as mechanical actuations, chemical reactions, optical, electrical and thermal schemes, light field distributions of these reconfigurable metasurfaces exhibit dynamically controllable functionalities, offering a programmable flexibility

*syxiao@ncu.edu.cn

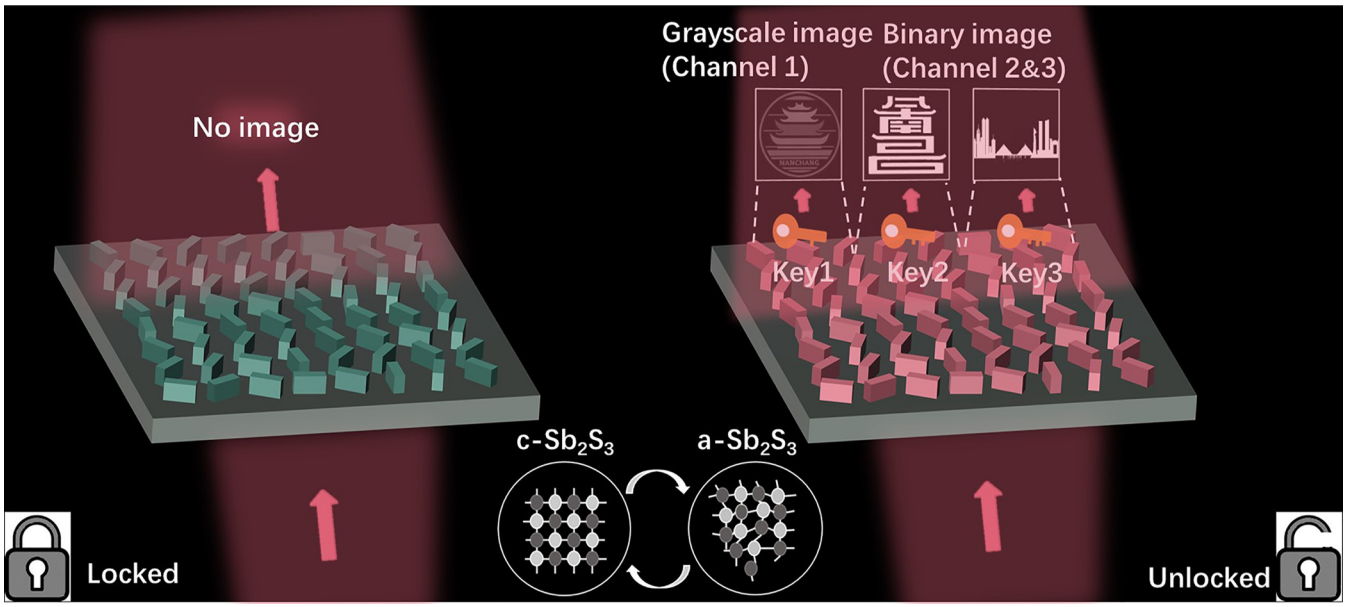

FIG. 1. Schematic diagrams of the designed single-sized metasurfaces based on Sb_2S_3 for dynamic three-channel nanoprinting imaging. The tunable metasurfaces display three different nanoprinting images using the polarization controls as the decoding keys under the amorphous states of Sb_2S_3 (a-Sb_2S_3) and hide the image information under the crystalline states of Sb_2S_3 (c-Sb_2S_3). The on and off modes can be switched reversibly between the two states.

in information processing and storage [46]. In particular, chalcogenide phase-change materials (PCMs) are uniquely poised for the photonic modulation and resonance tuning of reconfigurable metasurfaces, owing to their striking portfolio of properties [47–53]. PCMs can be rapidly and reversibly switched between amorphous and crystalline states, and the two states show pronounced contrast in optical and electronic properties. In recent studies, Sb_2S_3, Sb_2Se_3, and $GeSe_3$ have been identified as a family of highly promising ultralow-loss PCMs for nanophotonic devices over the visible and mid-infrared spectrum [54]. They have been successfully demonstrated in various reconfigurable metasurface devices for information storage and display such as high-resolution color [55–57], beam steering [58,59], and holographic display [60–62]. However, the realization for dynamic information multiplexing and encryption via single-sized phase-change metasurfaces remains unexplored.

In this paper, we propose a simple design approach, which enables dynamic intensity modulation for switchable three-channel nanoprinting imaging in a single-sized metasurface. Through elaborately controlling the orientation angles of an anisotropic Sb_2S_3 meta-atom governed by Malus's law, it creates the degeneracy of energy allocation in different channels and achieves nanoprinting information multiplexing in a single metasurface, allowing for metasurface encryption under the combinations of input/output polarization control. Different from the previous polarization-multiplexing metasurfaces based on orthogonal-polarization optical setup, the designed phase-change metasurface utilizes nonorthogonal input/output polarization combination of (0, 0) as an independent information channel, in addition to the orthogonal combinations of (0, $\pi/2$) and ($\pi/8$, $5\pi/8$) of the bulk-optic polarizer and analyzer in the optical path. The Sb_2S_3 amorphous-crystal phase transition provides active tunability of the three-channel nanoprinting imaging from switch on to off state, further improving the information security. In the design, by simply arranging the orientations of single-sized Sb_2S_3 meta-atoms on a single-layered metasurface, the three-channel nanoprinting images can be simultaneously recorded and dynamically switchable. Furthermore, the proposed metasurface shows the advantage of manifold information and multifold encryption, offering promising prospects for applications in high-secure and high-density optical storage, ultracompact and intelligent dynamic display, and optical information encryption.

II. DESIGN PRINCIPLE

Figure 1 schematically illustrates the designed phase-change metasurface, which enables dynamic control of multichannel nanoprinted display by adjusting the amorphous-crystal phase transition states of Sb_2S_3. The image information of three independent channels can be encoded into a single-sized phase-change metasurface, through carefully arranging the Sb_2S_3 nanobricks with a fixed size but different orientations to modulate light intensity pixel by pixel. In the amorphous state, the metasurface can be characterized by the amplitude profiles that encode the near-field information. Using corresponding polarization controls as the decoding keys, the three different nanoprinting images can be displayed at the transmission side. After Sb_2S_3 crystallizes from an amorphous state into an orthorhombic structure of fully crystalline state, the meta-atoms exhibit a substantial change in refractive index, and thus the image information encoded by amplitude modulation recorded on the metasurface cannot be read by arbitrary polarization keys. As a result, the nanoprinting display is switched into the off state in which the coded images are hidden. The switchable display driven by phase-change

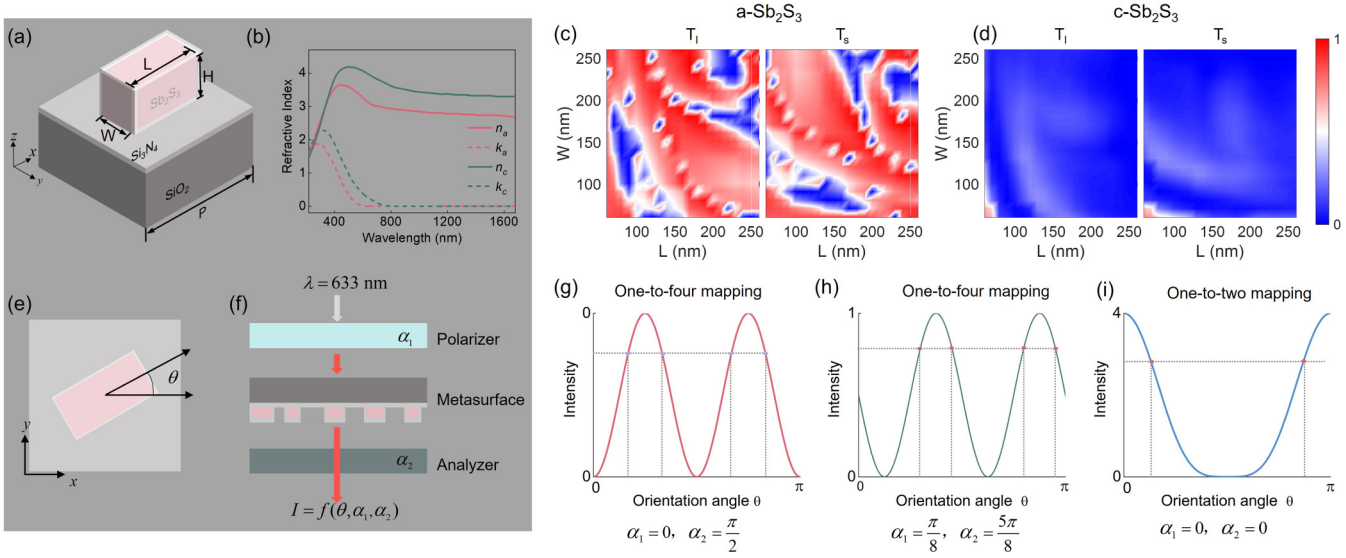

FIG. 2. Unit-cell structure and design principle. (a) Schematic illustration of a unit cell of the metasurfaces with defined structural parameters. (b) The refractive index of Sb_2S_3 for both amorphous and crystalline states [54]. [(c),(d)] Simulated transmission with incident light polarized along the long and short axes of the nanobrick of a-Sb_2S_3 and c-Sb_2S_3 metasurfaces, respectively. (e) Planar illustration of a unit cell with a rotation angle θ. (f) Principle of intensity modulation in near-field nanoprinted display. When the metasurfaces are inserted between a polarizer and analyzer, the transmission intensity varies with the rotation angle of the nanobrick θ, the polarization directions of polarizer and analyzer, i.e., α_1 and α_2. [(g)–(i)] The transmission intensity as a function of θ with $I_0 = 4$, as the polarization direction combinations of polarizer and analyzer are $(0, \pi/2)$, $(\pi/8, 5\pi/8)$, and $(0, 0)$, respectively.

meta-atoms affords another degree of freedom in information encryption.

In the phase-change metasurface structure for nanoprinted display, each unit cell is composed of a Sb_2S_3 nanobrick with fixed length L, width W, and height H sitting on a planar substrate SiO_2, as shown in Fig. 2(a). For practical fabrication and modulation, the nonreactive dielectric material, a Si_3N_4 film with a thickness of 70 nm is employed to encapsulate the Sb_2S_3 nanobricks [55,60]. Such configuration can create an undisturbed environment for stable performance of the nanostructures, and protect the chalcogenide material from the heat damage during the amorphous-crystal phase transition process such as avoiding sulfur loss through evaporation in thermal switching. Here we select Sb_2S_3 as a nonvolatile PCM to construct the metasurface operating in the visible spectrum. Compared to the most considered PCMs such as GST and VO_2, Sb_2S_3 has a wide bandgap of 1.70–2.05 eV, leading to the absorption band edge moving to the visible spectrum around 600 nm [63]. As shown in Fig. 2(b), the refractive index of a-Sb_2S_3 keeps high around 3.5 in the visible spectrum, being an excellent counterpart to the widely-used Si_3N_4 and TiO_2 for visible all-dielectric metasurfaces. The refractive index contrast between the amorphous and crystalline states is around 0.5 in both the real and imaginary components at the wavelength of interest $\lambda = 633$ nm, allowing dynamic switching of the optical properties. The amorphous and crystalline states of Sb_2S_3 can be reversibly and rapidly switched by external stimuli including thermal, electrical, and optical excitations. Complete crystallization of Sb_2S_3 nanostructures has been reported to be achieved in an argon(Ar)-filled furnace for one hour [55], and more effectively accomplished with electrical and laser pulses [60,64–66].

To create the encoding freedom for light polarization, the phase-change metasurface is inserted between a bulk-optic polarizer and an analyzer. As shown in Fig. 2(f), the incident light passes through a polarizer with polarization direction α_1, a nanobrick with rotation angle θ, and an analyzer with polarization direction α_2. According to Malus's law, a general expression of the amplitude (intensity) and polarization state of the output light can be written as

$$I = I_0 \left| \frac{t_l + t_s}{2} \cos(\alpha_2 - \alpha_1) + \frac{t_l - t_s}{2} \cos(2\theta - \alpha_2 - \alpha_1) \right|^2, \tag{1}$$

where I_0 is the light intensity after the polarizer, t_l and t_s are the complex transmission coefficients along the long and short axis of the nanobrick, respectively. The derivation of Eq. (1) can be found in the Appendix A. The output transmission amplitude can be regarded as a function dependent on the polarization direction α_1, α_2 and nanobrick orientation θ, and thus the amplitude modulation can be realized by carefully setting polarization combination and meta-atom orientation.

If the incident light is linearly polarized along x axis after polarizer with $\alpha_1 = 0$, and the output transmission light through the analyzer with $\alpha_2 = \pi/2$ is along the y axis, the amplitude in Eq. (1) can be calculated in a simple form as

$$I_1 = I_0 \left| \frac{t_l - t_s}{2} \right|^2 \sin^2(2\theta). \tag{2}$$

For the designed anisotropic nanobrick in Fig. 2(a), $|\frac{t_l - t_s}{2}|^2$ is usually considered as the cross-polarization conversion efficiency, and it can be set as a fixed value for nanobrick with specific dimensions. Here the transmission amplitude along the long and short axes are set as $T_l = 1$ and $T_s = 0$,

respectively. As a result, by adjusting the orientation θ of each meta-atom, the near-field amplitude can obtain continuous manipulation, and then a continuous grayscale image can be encoded into the metasurface pixel by pixel. This can be observed using the normalized curve depicted in Fig. 2(g). In particular, there is more than one choice of the orientation angle, including θ, $\pi/2-\theta$, $\pi/2+\theta$, and $\pi-\theta$, to generate a specific output amplitude. Such orientation degeneracy offers degrees of freedom in designing meta-atoms to establish multiple information channels. In the second near-field channel, we set $\alpha_1 = \pi/8$ and $\alpha_2 = 5\pi/8$ respectively, written in the form of $(\pi/8, 5\pi/8)$. The output transmission amplitude in Eq. (1) can be calculated as

$$I = I_0 \left| \frac{t_l - t_s}{2} \right|^2 \sin^2(2\theta - \pi/4). \tag{3}$$

As depicted in Fig. 2(h), the orientation degeneracy with one-to-four mapping still works for such polarization control. Then we introduce the third channel by setting $\alpha_1 = 0$ and $\alpha_2 = 0$ with the transmission amplitude calculated as

$$I = I_0 \left| \frac{t_l - t_s}{2} \sin(2\theta) + \frac{t_l + t_s}{2} \right|^2. \tag{4}$$

With $T_l = 1$ and $T_s = 0$, Eq. (4) can be simplified as $I = \frac{I_0}{4}(\sin(2\theta)+1)^2$. As depicted in Fig. 2(i), it can be observed that the amplitude curve shows a one-to-two mapping degeneracy with quite different tendency compared with those in Figs. 2(g) and 2(h). Such polarization combination of polarizer and analyzer brings another way to modulate amplitude in the new channel.

The three equations form the basis for realizing multifold integration and dynamic display of nanoprinting images with a single-sized phase-change metasurface design approach. To be exact, the fundamental of this approach lies in intelligently engineering the amplitude of incident waves under polarization controls. Based on the degeneracy of energy allocation governed by Malus's law, the multiplexing information channel can be established by varying nanobrick orientation and controlled by polarization combinations. Meanwhile, dynamically tunable display can be realized by adjusting the crystalline state of Sb_2S_3 meta-atoms under thermal, electrical, or optical external stimuli. The three channels are controlled by the combinations of $(0, \pi/2)$, $(\pi/8, 5\pi/8)$, and (0, 0) of polarizer and analyzer in the optical path, and it is interesting that the nonorthogonal polarization optical setup, i.e., the input/output polarization combination of (0, 0) is different from the usual case of metasurface-based polarization multiplexing conducted in orthogonal polarization optical path. Such polarization multiplexing metasurface takes full advantage of the orientation degeneracy of Malus's law and employs polarization as the decrypted keys to improve the information capacity and security.

III. RESULTS AND DISCUSSION

To achieve the best polarization-controlled energy allocation efficiency, the physical dimensions of the Sb_2S_3 meta-atoms are optimized at the operating wavelength of 633 nm. The period of the unit cell is selected as $P = 400$ nm to avoid the unwanted high-order diffraction. The physical parameters including length and width of the nanobrick is optimized by keeping the period and the height $H = 550$ nm fixed. The simulated transmission efficiencies along the long and short axis are depicted in Figs. 2(c) and 2(d) for the a-Sb_2S_3 and c-Sb_2S_3, using the finite-difference-time-domain (FDTD) method. As a result, the designed Sb_2S_3 nanobrick is 170 nm in length and 250 nm in width, with the maximum transmission along the nanobrick's long-axis direction (∼98%) and the minimum transmission along the short-axis direction (∼0.1%) for a-Sb_2S_3. At the same time, both the transmission amplitudes for c-Sb_2S_3 are compressed to be a very low value (near zero), fulfilling the dynamic display of switching on and off.

To verify our proposed design approach, we first consider a simple case in which the phase-change metasurfaces achieve dynamic display of the two-channel nanoprinting images, as detailed in Appendix B. Furthermore, taking full advantage of orientation degeneracy for amplitude responses, we are able to independently encode the three-channel nanoprinted display into a single-sized phase-change metasurface. Figure 3 illustrates the metasurface design flow for synchronizing display of three different images. Here the intensity modulation based on Eqs. (2)–(4) is adopted corresponding to channel 1, 2, and 3, respectively. The continuous grayscale image of Tengwang Pavilion, which is one of the most famous tower in China, is encoded in channel 1, while the binary image of Nanchang city is encoded in channel 2, and the binary image of buildings besides Ganjiang River encoded in channel 3. The amplitude profiles for 40×40 μm^2 metasurface are numerically calculated. The key of multiplexed amplitude modulation is the nanobrick orientation distribution of the single-sized metasurface that simultaneously satisfies the requirements for the three-channel displays. From the working principle, we elaborate the orientation encoding strategy of the three-channel images in Table I. Based on the amplitude modulation function of I_1, I_2, and I_3, the orientation angles θ are divided into four sections. In each section, I_1 can achieve a continuous amplitude modulation ranging from 0 ∼ 1. In sections 1 and 3, I_2 obtains amplitude modulation lower than 0.5, while it is higher than 0.5 in sections 2 and 4. For convenience we take the lower and higher values as the binary code of "0" and "1" respectively. In a similar way, I_3 with lower amplitude in section 2 and 3 can be considered as the "0", while higher amplitude in section 1 and 4 as "1". With these intuitive relations resulting from the orientation degeneracy, the orientation of each nanobrick can be determined to meet the requirement for all the three channels. As a result, a continuous grayscale image and two binary images can be encoded into the same metasurface but displayed in three information channels under corresponding polarization control.

The design flow is described in detail in Fig. 3. With the amplitude profile of the selected continuous grayscale image of Tengwang Pavilion, the four orientation candidates can be obtained for I_1 using Eq. (2) for Malus's law degeneracy. To program the second channel information, the amplitude of the target image, which is initially binarized, is calculated for selecting the nanobrick orientations. According to the look-up relations in Table I, two of the candidates can be determined for a lower value of "0" or a higher value of "1". Eventually,

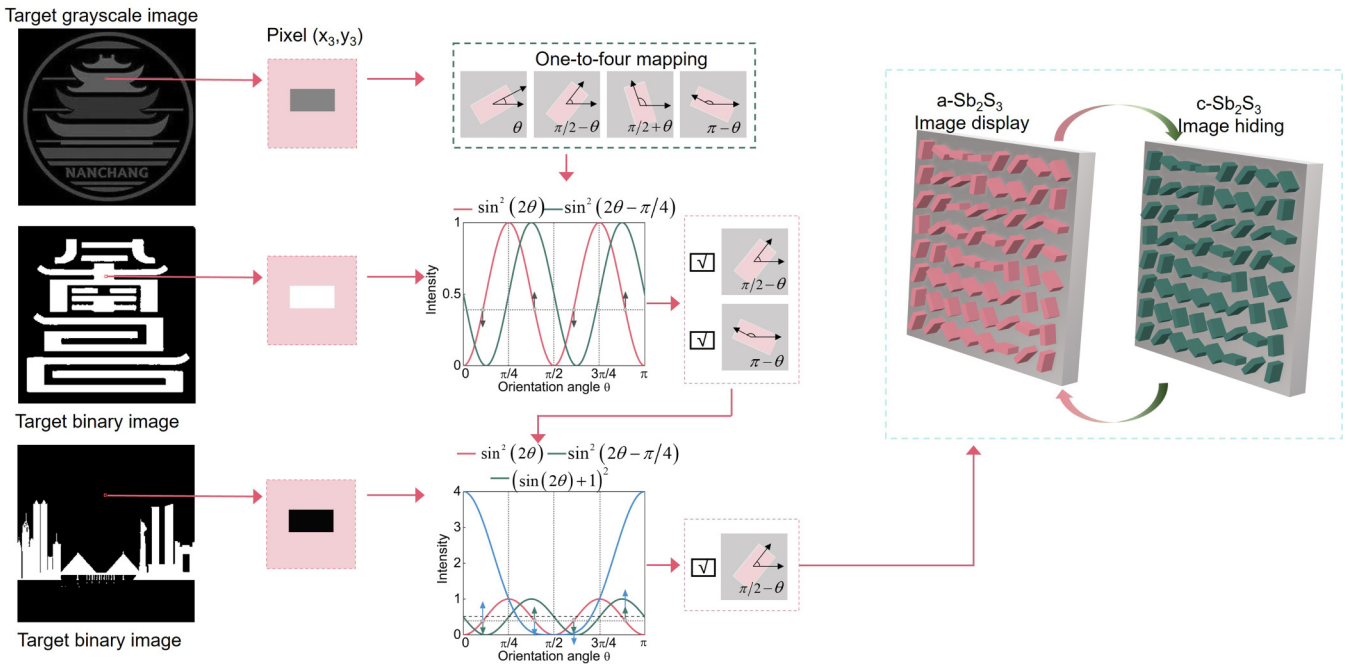

FIG. 3. Flowchart of designing the proposed three-channel phase-change metasurface. One continuous grayscale image and two binary images are chosen to encode the orientation distributions into a single-sized metasurface. Owing to the orientation degeneracy, the unit-cell amplitude of the first channel corresponds to four orientations, including θ, $\pi/2-\theta$, $\pi/2+\theta$, and $\pi-\theta$ where θ is assumed to belong in the interval $[0, \pi/4]$, and the four orientations are associated with Sections 1-4 in Table I, respectively. Then two of them are selected to encode the amplitude of the second channel. At last, only one of the orientations can be determined to meet the requirement for the third channel. After the determination of the orientation distribution, a three-channel metasurface can be obtained.

owing to the one-to-two mapping relations of I_3 amplitude modulation, only one of the orientation candidates is chosen to further satisfy the amplitude encoding of the target binary images in the third channel. In this way, the orientations of nanostructures can be determined pixel by pixel by combining the three-channel amplitude modulation for target images, and the phase-change metasurface is designed to meet the amplitude modulation requirement for the three channels.

Based on the design scheme above, the three different grayscale images are encoded into a single-sized phase-change metasurface. The metasurface composed of 100×100 unit cells is simulated using FDTD method at the operating wavelength at 633 nm. As shown in Fig. 4, the designed single-sized metasurface realizes the three-channel and dynamically tunable nanoprinting image display. When the designed metasurface is inserted between the polarizer and analyzer, different images in the three channels can only be observed clearly under the preset polarization combinations. By setting the polarization directions of polarizer and analyzer as $(0, \pi/2)$, $(\pi/8, 5\pi/8)$, and $(0, 0)$ respectively, the three-channel images including a continuous grayscale image of Tengwang Pavilion, a binary image of Nanchang city, and a binary image of buildings are observed in a-Sb_2S_3 metasurface, as depicted in the first row of Fig. 4. The decoded images are clear with high resolution and fidelity, implying the three-channel amplitude modulation works well with the design scheme. Meanwhile, because the light amplitude for binary images in channel 2 and 3 can only be modulated as higher or lower values, not the exactly 1 or 0, and the final orientation is selected from the four candidates for the continuous grayscale image of Tengwang Pavilion, image display in channel 2 and 3 might be accompanied by the appearance of the image in channel 1 as shallow background. Subsequently, we successfully realize the dynamic switch of

TABLE I. Transmission amplitude under the polarization direction combinations of polarizer and analyzer of $(0, \pi/2)$, $(\pi/8, 5\pi/8)$, and $(0, 0)$, with the incident light intensity I_0 setting as 4.

θ Sections	$I_1 = \sin^2(2\theta)$	$I_2 = \sin^2(2\theta - \pi/4)$	$I_3 = (\sin(2\theta) + 1)^2$
1: $[0, \pi/4]$	[0,1]	[0,0.5]: "0"	[1,4]: "1"
2: $[\pi/4, \pi/2]$	[0,1]	[0.5,1]: "1"	[0,1]: "0"
3: $[\pi/4, 3\pi/4]$	[0,1]	[0,0.5]: "0"	[0,1]: "0"
4: $[3\pi/4, \pi]$	[0,1]	[0.5,1]: "1"	[1,4]: "1"

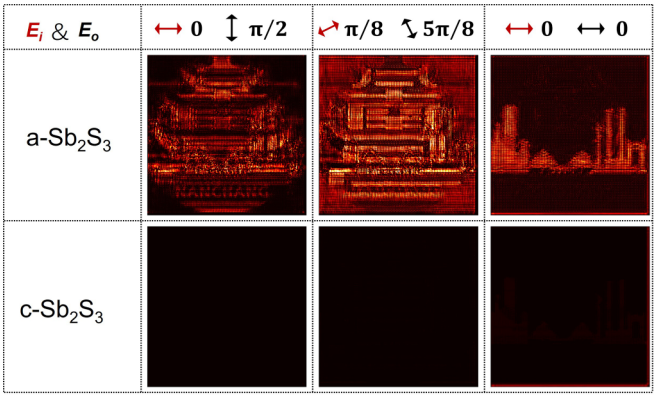

FIG. 4. Simulated near-field results of the three-channel metasurface. Using the corresponding polarization combinations as the decoding keys, three different nanoprinting images of the designed metasurfaces are displayed, and dynamically switched in a-Sb_2S_3 and c-Sb_2S_3 metasurfaces.

nanoprinting display from on to off mode via changing the crystalline state of Sb_2S_3 metasurface, as depicted in the second row. As the Sb_2S_3 is phase transitioned to fully crystalline state, the transmission efficiency is largely varied with two orders of magnitude reduction, due to the refractive index contrast of $\Delta n \sim 0.8$ and $\Delta k \sim 0.3$. Such significant modulation depth for amplitude profile suggests large switch ratio of the three-channel images. Hence the preset images are hidden for c-Sb_2S_3 metasurface. Specially, Sb_2S_3 can be easily and reversibly switched via external stimuli between its amorphous and crystalline states. Benefiting from these characteristics, the phase-change metasurface can dynamically and reversibly switch the image displays between the on and off mode, implementing the image information display and encryption during the process. The fabrication procedure of the Sb_2S_3 metasurface is briefly described in Appendix C. In addition, the sensitivity of the images to the deviations in wavelength and polarization combination around the designed values are also discussed in Appendices D and E.

IV. CONCLUSIONS

In conclusion, we have proposed and demonstrated a simple design strategy for a phase-change metasurface enabling dynamic three-channel amplitude modulation. Unlike previous multiplexing approaches such as the multilayer, super-cell approaches, and the single-cell nanostructures with different meta-atom dimensions, the proposed strategy employs a single-sized Sb_2S_3 meta-atom to encode multiple near-field information on the metasurface interface. By combining the orientation degeneracy of the amplitude modulation with polarization control, the proposed design strategy provides great freedom to independently manipulate each near-field channel for information encoding. As a consequence, three different nanoprinting images can be displayed using the corresponding polarization control as decoding keys. Leveraging the tunable optical properties of Sb_2S_3, the multiplexed information channels can be switched between on and off mode. Such phase-change metasurfaces provide a unique solution to realize dynamic and multifold information multiplexing and encryption without decreasing the image resolution and burdening the nanostructure design and fabrication. With the unparalleled advantages such as ultracompactness, simple design and fabrication technique, high information density, and high resolution display, the proposed metasurfaces suggest significant potential in many applications like high-dense optical data storage, ultracompact image displays, and information encryption/security.

ACKNOWLEDGMENTS

This work was supported by the National Natural Science Foundation of China (Grants No. 12364045, No. 12264028, and No. 12304420), the Natural Science Foundation of Jiangxi Province (Grants No. 20232BAB201040 and No. 20232BAB211025), the Sichuan Science and Technology Program (Grant No. 2023ZYD0020), the Chenguang Program of Shanghai Education Development Foundation and Shanghai Municipal Education Commission (Grant No. 21CGA55), the Young Elite Scientists Sponsorship Program by JXAST (Grant No. 2023QT11), and the Sichuan Provincial Central Leading Local Science and Technology Development Special Project (Grant No. 2023ZYD0020).

APPENDIX A: DERIVATION OF THE AMPLITUDE MANIPULATION OF A SINGLE-SIZED META-ATOM FROM JONES MATRIX

Each anisotropic meta-atom shown in Fig. 2(a) can be considered as a Jones matrix connecting the input field to the output field, and the relation between the input and output electric fields for normal incidence can be expressed as $|E_o\rangle = J|E_i\rangle$. When the meta-atom is rotated by angle θ with respect to the x direction, the transmission Jones matrix of the nanobrick can be expressed by

$$\begin{aligned} J(\theta) &= R(\theta)\begin{bmatrix} t_l & 0 \\ 0 & t_s \end{bmatrix} R(-\theta) \\ &= \begin{bmatrix} \cos\theta & -\sin\theta \\ \sin\theta & \cos\theta \end{bmatrix}\begin{bmatrix} t_l & 0 \\ 0 & t_s \end{bmatrix}\begin{bmatrix} \cos\theta & \sin\theta \\ -\sin\theta & \cos\theta \end{bmatrix}, \end{aligned} \tag{A1}$$

where $R(\theta)$ is the rotation matrix, t_l and t_s are the complex transmission coefficients along the long and short axis of the nanobrick, respectively.

When the light passes through a bulk-optic polarizer, the nanobrick, and an analyzer, the Jones vector of the transmission light can be calculated as

$$\begin{aligned} |E_o\rangle &= \begin{bmatrix} \cos^2\alpha_2 & \sin\alpha_2\cos\alpha_2 \\ \sin\alpha_2\cos\alpha_2 & \sin^2\alpha_2 \end{bmatrix} J(\theta)|E_i\rangle \\ &= A_i\left(\frac{t_l + t_s}{2}\cos(\alpha_2 - \alpha_1) + \frac{t_l - t_s}{2}\cos(2\theta - \alpha_2 - \alpha_1)\right) \\ &\quad \times \begin{bmatrix} \cos\alpha_2 \\ \sin\alpha_2 \end{bmatrix}, \end{aligned} \tag{A2}$$

where α_2 is the polarization direction of the analyzer, i.e., the angle between the analyzer's transmission axis and x axis. The incident light field is $|E_i\rangle = [A_i\cos\alpha_1\ A_i\sin\alpha_1]^T$, where A_i denotes the amplitude of the incident light after passing through the bulk polarizer, and α_1 is the polarization direction

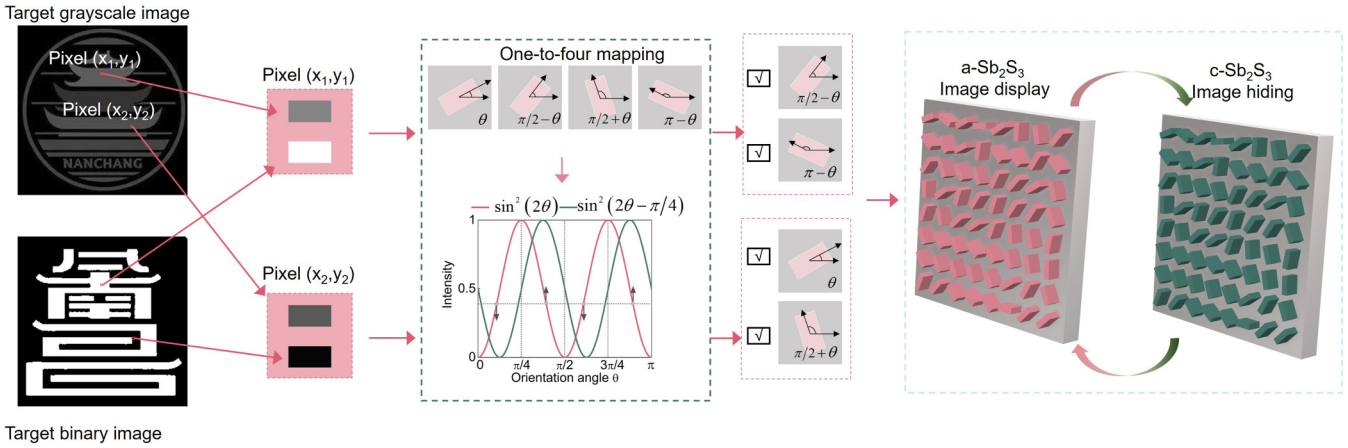

FIG. 5. Detailed design flow diagram of the phase-change metasurface for two-channel nanoprinting displays. First, a continuous grayscale image and a binary image are selected and their amplitude distributions are calculated. Then the pixel amplitude of the continuous grayscale image is discretized into four orientations, including θ, $\pi/2-\theta$, $\pi/2+\theta$, and $\pi-\theta$, where θ is assumed to belong in the interval [0, $\frac{\pi}{4}$], and the four orientations are associated with Sections 1–4 in Table I, respectively. The two of them are selected to simultaneously meet the amplitude modulation for the binary image. By carefully selecting required orientations pixel by pixel, the two-channel nanoprinting metasurface is designed.

of the polarizer. According to Eq. (A2), the transmission light is polarized along the transmission axis of the analyzer, and the intensity in transmission can be expressed by

$$I = I_0 \left| \frac{t_l + t_s}{2} \cos(\alpha_2 - \alpha_1) + \frac{t_l - t_s}{2} \cos(2\theta - \alpha_2 - \alpha_1) \right|^2, \tag{A3}$$

where I_0 is the incident light intensity, $I_0 = |A_i|^2$. On the basis of Eq. (A3), the intensity distribution of the transmitted light field can be designed pixel by pixel. The equations here demonstrate the general case of the intensity modulation of the nanobrick. In the main text, we consider three cases: (1) $\alpha_1 = 0$, $\alpha_2 = \frac{\pi}{2}$; (2) $\alpha_1 = \frac{\pi}{8}$, $\alpha_2 = \frac{5\pi}{8}$; (3) $\alpha_1 = 0$, $\alpha_2 = 0$; and then the intensity modulations under these polarization controls build up three different information channels.

APPENDIX B: DYNAMIC DISPLAY OF A TWO-CHANNEL NANOPRINTING METASURFACES

Considering the amplitude difference and the orientation degeneracy from Eqs. (2) and (3), it is viable to design metasurface with appropriate orientation distribution for coding two grayscale images. Figure 5 illustrates the two-channel metasurface design flow. Here the intensity modulation based on Eqs. (2) and (3) is adopted to encode the information in channel 1 and 2 respectively. The continuous grayscale image of Tengwang Pavilion is encoded in channel 1 and the binary image of Nanchang city is encoded in channel 2. The reasonable orientation distributions that simultaneously satisfy the amplitude modulation requirements for the two-channel displays are necessary. Combing the difference of transmission amplitudes, the orientation angles θ are divided into four sections in Table I. In each section, I_1 can achieve a continuous amplitude modulation ranging from $0 \sim 1$, while I_2 exhibits a lower or higher than 0.5 amplitude to form a two-step binary image. In this regard, the channel 1 enables a continuous modulation, and the channel 2 realizes a binary pattern modulation by choosing the values lower and higher than 0.5. For example, for I_1 of the continuous grayscale image at the pixel $(x1, y1)$, the four candidate can be calculated by θ_1, $\pi/2-\theta_1$, $\pi/2+\theta_1$, and $\pi-\theta_1$. To achieve I_2 for binary image of "1" with a high value, the orientations of $\pi/2-\theta_1$ and $\pi-\theta_1$ can be selected at this pixel. In contrast, at the pixel $(x2, y2)$, the orientations of θ_2 and $\pi/2+\theta_2$ can be selected to achieve I_2 of "0" with a low value. Therefore, by combining the two-channel amplitude modulation for target images, the orientations of nanostructures can be determined pixel by pixel, and the multiplexed phase-change metasurface can be formed.

The two-channel metasurface composed of 100×100 unit cells is designed and simulated. As shown in Fig. 6, the designed single-sized metasurface realizes the dynamically tunable two-channel nanoprinting displays. When the incident light passes through the polarizer, metasurfaces and analyzer, different images can only be observed clearly under specific polarization combinations of polarizer and analyzer. It is obvious that the simulation results match well with the encoded images. Moreover, as Sb_2S_3 metasurface experiences the phase transition from amorphous to crystalline state, the image amplitudes obtain significant decrease with images switching from on to off mode. Such dynamic tunability of designed metasurface can also be attributed to significant change in transmission due to gradually increasing refractive index of Sb_2S_3 in both real and imaginary components.

APPENDIX C: FABRICATION PROCEDURE OF THE Sb_2S_3 METASURFACE

The fabrication of the nanostructured Sb_2S_3 metasurfaces can be conducted using the procedures listed in Fig. 7. At first, Sb_2S_3 film with the required thickness is deposited onto the glass substrate via radio frequency (RF) sputtering. The

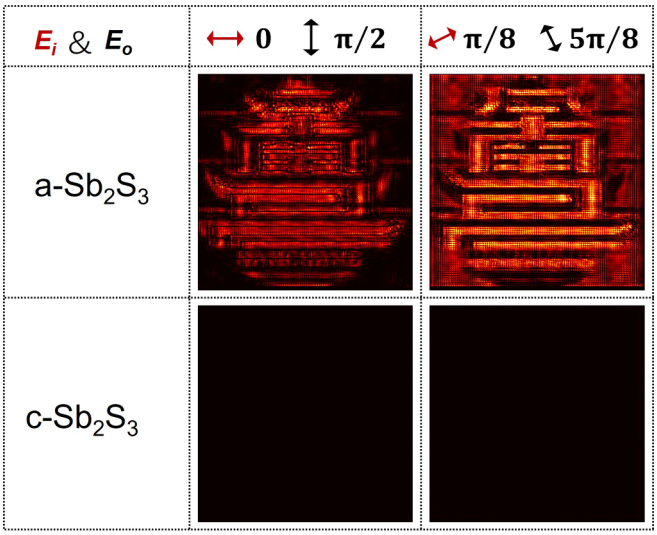

FIG. 6. Simulated near-field results of the two-channel metasurface. Using the corresponding polarization combinations as the decoding keys, two different nanoprinting images of the designed metasurfaces are displayed, and dynamically switched in a-Sb_2S_3 and c-Sb_2S_3 metasurfaces.

poly methyl methacrylate (PMMA) resist is spin coated onto the structure and then baked. After the electron beam exposure (EBL), the PMMA sample is developed with rectangular patterns. A 20-nm-thick Pd film is evaporated onto the PMMA resist, followed by the lift off process to remove the resist. The patterned structures are transferred to the Sb_2S_3 film using inductively coupled plasma (ICP). To protect Sb_2S_3 nanostructures during the phase transition, a 70-nm-thick Si_3N_4 film is deposited conformally using ICP chemical vapor decomposition (CVD) to encapsulate the Sb_2S_3 array.

APPENDIX D: IMAGE DISPLAY AT DIFFERENT OPERATING WAVELENGTHS

Because of the fact that the refractive index of the adopted Sb_2S_3 materials vary as a function of wavelength as shown in Fig. 2(b), it can be expected that the performance of dynamic intensity modulation would deviate from the case at 633 nm. To study the sensitivity of the images to variations in operating wavelength (λ), we consider the dynamic image display in

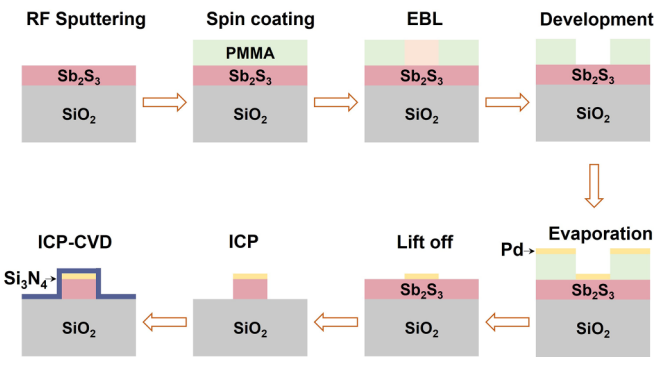

FIG. 7. Fabrication flow chart of the proposed Sb_2S_3 metasurfaces.

the designed metasurfaces composed of 100 × 100 unit cells under a broadband wavelength regime ranging from 450 nm to 850 nm. The simulation results for channel 1 at different wavelengths are depicted in Fig. 8. For 450 nm and 550 nm, the images of both a-Sb_2S_3 and c-Sb_2S_3 metasurfaces cannot be observed. This can be attributed to the quite low transmission efficiency due to the lossy a-Sb_2S_3 and c-Sb_2S_3 at the two wavelengths, for example, the imaginary parts of refractive index k at 450 nm are 0.7 and 1.41 for the amorphous and crystalline states, respectively. When the incident wavelength is 600 nm, the grayscale image of Tengwang Pavilion begins to appear at a-Sb_2S_3 metasurface with a low intensity and disappear at c-Sb_2S_3 metasurface, showing dynamical switch functionality. The switchable image can also be observed at 660 nm. Because of the large deviation of the refractive index at 690 nm relatively to the index at the selected wavelength 633 nm, the image at amorphous state becomes indistinct, even though of image of c-Sb_2S_3 metasurface remains on the off mode. In contrast, the image information with low intensity can be faintly observed for both states at 750 nm and 850 nm, as shown in Fig. 8. This can also be reasoned by the variations of refractive index of Sb_2S_3. When incident wavelength shifts to the 750 nm and 850 nm, the real part n of refractive index of Sb_2S_3 shows slight variations, even becomes stable in the near infrared regime, and the values of k is around 0 within this wavelength regime. At the two wavelengths, image information can be maintained but the image quality shows deterioration. During the wavelength shift, n begins to approach the value of a-Sb_2S_3 at 633 nm, and both a-Sb_2S_3 and c-Sb_2S_3 is lossless within this wavelength regime. As a consequence, images information for both states simultaneously appear. The designed metasurface loses its dynamic functionality to switch on and off images due to the low refractive contrast between amorphous and crystalline states.

APPENDIX E: SENSITIVITY OF IMAGES TO THE ORIENTATIONS OF THE POLARIZER AND ANALYZER

We further explore the sensitivity of the images to the orientations of the polarizer and analyzer (α_1, α_2) around the designed values, as shown in Fig. 9. It can be observed that, when α_1 and α_2 deviate from the designed values, different degrees of crosstalk occurs and the target images cannot be observed clearly. For example, in the first column of Fig. 9, the image of Tengwang Pavilion in channel 1 and the image of buildings besides Ganjiang River in channel 3 can be simultaneously distinguished. The images are overlapped and show obscure patterns in the same transmitted plane. For the all cases in the Fig. 9 where the input/output polarization combinations (α_1, α_2) deviate from the designed values, the image quality of the observed pattern is lowered down. The sensitivity of the three-channel nanoprinting images to the polarization orientations of polarizer and analyzer can be revealed by Eq. (1) of the main text. With the general expression of the amplitude and polarization control in Eq. (1), the output transmission amplitude can be regarded as a function dependent on the polarization directions of polarizer α_1 and analyzer α_2, and nanobrick orientation θ. By elaborately setting these polarization combination and meta-atom

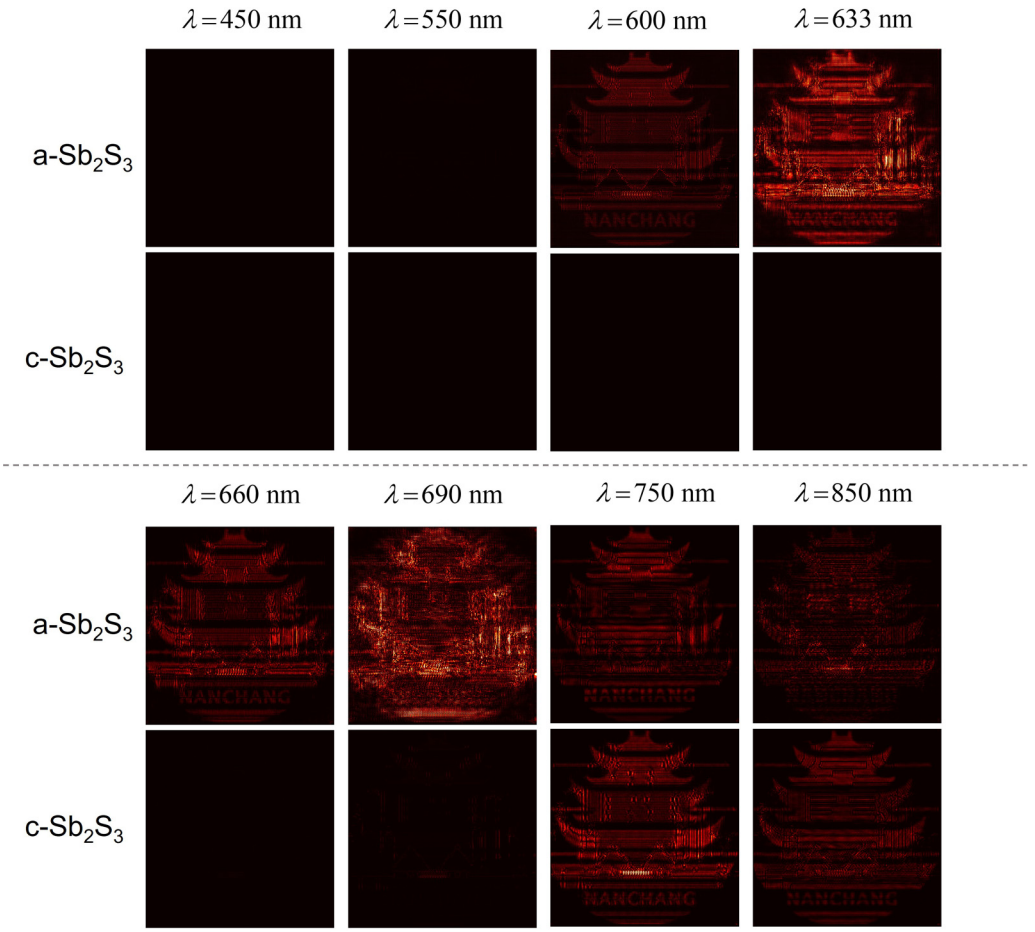

FIG. 8. Simulated near-field results in channel 1 of the designed metasurface at different wavelengths of 450 nm, 550 nm, 600 nm, 660 nm, 690 nm, 750 nm, 850 nm, alongside the results for the designed wavelength of 633 nm.

orientation, the metasurface can simultaneously record and encode different images of three channel. When an arbitrary polarization combination is imparted to the metasurface with specific orientation distribution, the transmission amplitude in each channel would not obtain the independent modulation, as justified by the results in Fig. 9.

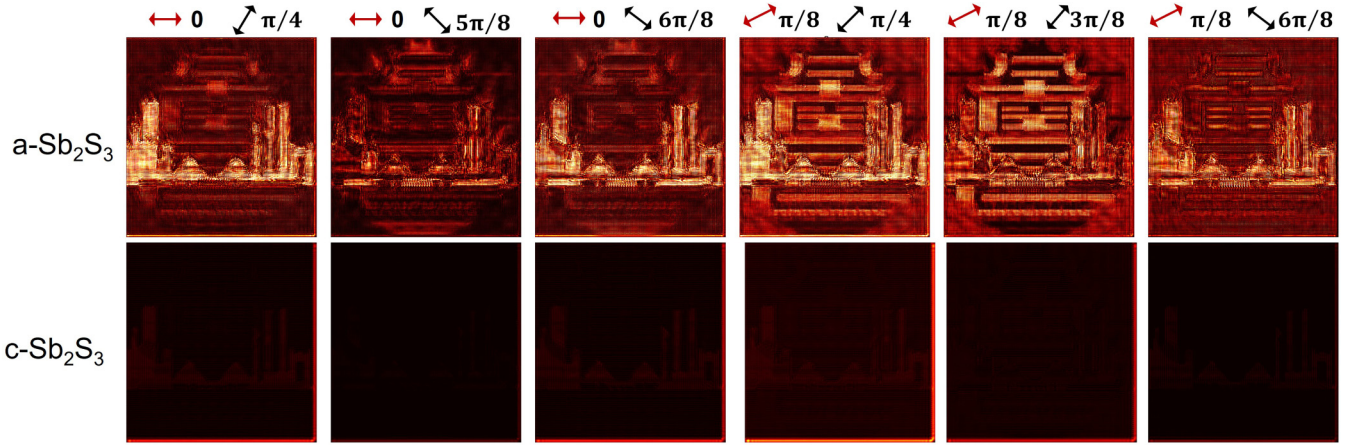

FIG. 9. Simulated near-field results of the designed metasurfaces when the polarization combinations of the bulk-optic polarizer and analyzer deviate from the designed values.

[1] N. Yu, P. Genevet, M. A. Kats, F. Aieta, J.-P. Tetienne, F. Capasso, and Z. Gaburro, Light propagation with phase discontinuities: generalized laws of reflection and refraction, Science **334**, 333 (2011).

[2] S. Sun, Q. He, S. Xiao, Q. Xu, X. Li, and L. Zhou, Gradient-index meta-surfaces as a bridge linking propagating waves and surface waves, Nat. Mater. **11**, 426 (2012).

[3] A. V. Kildishev, A. Boltasseva, and V. M. Shalaev, Planar photonics with metasurfaces, Science **339**, 1232009 (2013).

[4] S. M. Kamali, E. Arbabi, A. Arbabi, and A. Faraon, A review of dielectric optical metasurfaces for wavefront control, Nanophotonics **7**, 1041 (2018).

[5] D. Neshev and I. Aharonovich, Optical metasurfaces: New generation building blocks for multi-functional optics, Light Sci. Appl. **7**, 58 (2018).

[6] C. Wan, C. Dai, J. Zhang, S. Wan, Z. Li, G. Zheng, X. Zhang, and Z. Li, 3D meta-prisms for versatile beam steering by hybridizing plasmonic and diffractive effect in the broadband visible regime, Small **17**, 2100561 (2021).

[7] P. Thureja, G. K. Shirmanesh, K. T. Fountaine, R. Sokhoyan, M. Grajower, and H. A. Atwater, Array-level inverse design of beam steering active metasurfaces, ACS Nano **14**, 15042 (2020).

[8] M. Khorasaninejad, W. T. Chen, R. C. Devlin, J. Oh, A. Y. Zhu, and F. Capasso, Metalenses at visible wavelengths: Diffraction-limited focusing and subwavelength resolution imaging, Science **352**, 1190 (2016).

[9] R. J. Lin, V.-C. Su, S. Wang, M. K. Chen, T. L. Chung, Y. H. Chen, H. Y. Kuo, J.-W. Chen, J. Chen, Y.-T. Huang *et al.*, Achromatic metalens array for full-colour light-field imaging, Nat. Nanotechnol. **14**, 227 (2019).

[10] R. Jin, L. Tang, J. Li, J. Wang, Q. Wang, Y. Liu, and Z.-G. Dong, Experimental demonstration of multidimensional and multifunctional metalenses based on photonic spin hall effect, ACS Photon. **7**, 512 (2020).

[11] J. Li, C. Zheng, J. Li, G. Wang, J. Liu, Z. Yue, X. Hao, Y. Yang, F. Li, T. Tang, Y. Zhang, Y. Zhang, and J. Yao, Terahertz wavefront shaping with multi-channel polarization conversion based on all-dielectric metasurface, Photon. Res. **9**, 1939 (2021).

[12] J. Li, J. Li, Z. Yue, C. Zheng, G. Wang, J. Liu, H. Xu, C. Song, F. Yang, H. Li *et al.*, Structured vector field manipulation of terahertz wave along the propagation direction based on dielectric metasurfaces, Laser Photon. Rev. **16**, 2200325 (2022).

[13] A. Arbabi and A. Faraon, Advances in optical metalenses, Nat. Photon. **17**, 16 (2023).

[14] Z. Huang, Y. Zheng, J. Li, Y. Cheng, J. Wang, Z.-K. Zhou, and L. Chen, High-resolution metalens imaging polarimetry, Nano Lett. **23**, 10991 (2023).

[15] X. Ling, X. Zhou, K. Huang, Y. Liu, C.-W. Qiu, H. Luo, and S. Wen, Recent advances in the spin Hall effect of light, Rep. Prog. Phys. **80**, 066401 (2017).

[16] S. Li, X. Li, G. Wang, S. Liu, L. Zhang, C. Zeng, L. Wang, Q. Sun, W. Zhao, and W. Zhang, Multidimensional manipulation of photonic spin Hall effect with a single-layer dielectric metasurface, Adv. Opt. Mater. **7**, 1801365 (2019).

[17] K. Chaudhuri, A. Shaltout, D. Shah, U. Guler, A. Dutta, V. M. Shalaev, and A. Boltasseva, Photonic spin Hall effect in robust phase gradient metasurfaces utilizing transition metal nitrides, ACS Photon. **6**, 99 (2019).

[18] W. Zhu, R. Yang, G. Geng, Y. Fan, X. Guo, P. Li, Q. Fu, F. Zhang, C. Gu, and J. Li, Titanium dioxide metasurface manipulating high-efficiency and broadband photonic spin Hall effect in visible regime, Nanophotonics **9**, 4327 (2020).

[19] M. Kim, D. Lee, Y. Yang, Y. Kim, and J. Rho, Reaching the highest efficiency of spin Hall effect of light in the near-infrared using all-dielectric metasurfaces, Nat. Commun. **13**, 2036 (2022).

[20] L. Huang, X. Chen, H. Mühlenbernd, H. Zhang, S. Chen, B. Bai, Q. Tan, G. Jin, K.-W. Cheah, C.-W. Qiu *et al.*, Three-dimensional optical holography using a plasmonic metasurface, Nat. Commun. **4**, 2808 (2013).

[21] H. Ren, X. Fang, J. Jang, J. Bürger, J. Rho, and S. A. Maier, Complex-amplitude metasurface-based orbital angular momentum holography in momentum space, Nat. Nanotechnol. **15**, 948 (2020).

[22] Y. Bao, L. Wen, Q. Chen, C.-W. Qiu, and B. Li, Toward the capacity limit of 2D planar Jones matrix with a single-layer metasurface, Sci. Adv. **7**, eabh0365 (2021).

[23] M. Liu, W. Zhu, P. Huo, L. Feng, M. Song, C. Zhang, L. Chen, H. J. Lezec, Y. Lu, A. Agrawal, and T. Xu, Multifunctional metasurfaces enabled by simultaneous and independent control of phase and amplitude for orthogonal polarization states, Light Sci. Appl. **10**, 107 (2021).

[24] B. Xiong, Y. Liu, Y. Xu, L. Deng, C.-W. Chen, J.-N. Wang, R. Peng, Y. Lai, Y. Liu, and M. Wang, Breaking the limitation of polarization multiplexing in optical metasurfaces with engineered noise, Science **379**, 294 (2023).

[25] Z. Li, C. Chen, Z. Guan, J. Tao, S. Chang, Q. Dai, Y. Xiao, Y. Cui, Y. Wang, S. Yu *et al.*, Three-channel metasurfaces for simultaneous meta-holography and meta-nanoprinting: A single-cell design approach, Laser Photon. Rev. **14**, 2000032 (2020).

[26] J. Deng, L. Deng, Z. Guan, J. Tao, G. Li, Z. Li, Z. Li, S. Yu, and G. Zheng, Multiplexed anticounterfeiting meta-image displays with single-sized nanostructures, Nano Lett. **20**, 1830 (2020).

[27] R. Fu, K. Chen, Z. Li, S. Yu, and G. Zheng, Metasurface-based nanoprinting: principle, design and advances, Opto-Electron. Sci. **1**, 220011 (2022).

[28] Q. Dai, G. Zhu, W. Zhang, J. Li, Z. Li, H. Cui, K. Wei, Z. He, Z. Guan, and G. Zheng, Dual-channel anticounterfeiting color-nanoprinting with a single-size nanostructured metasurface, Opt. Express **30**, 33574 (2022).

[29] Q. Wei, B. Sain, Y. Wang, B. Reineke, X. Li, L. Huang, and T. Zentgraf, Simultaneous spectral and spatial modulation for color printing and holography using all-dielectric metasurfaces, Nano Lett. **19**, 8964 (2019).

[30] R. Chen, Y. Zhou, W. Chen, R. Chen, N. Iqbal, and Y. Ma, Multifunctional metasurface: Coplanar embedded design for metalens and nanoprinted display, ACS Photon. **7**, 1171 (2020).

[31] Y. Zhou, I. I. Kravchenko, H. Wang, J. R. Nolen, G. Gu, and J. Valentine, Multilayer noninteracting dielectric metasurfaces for multiwavelength metaoptics, Nano Lett. **18**, 7529 (2018).

[32] Y. Hu, X. Luo, Y. Chen, Q. Liu, X. Li, Y. Wang, N. Liu, and H. Duan, 3D-integrated metasurfaces for full-colour holography, Light Sci. Appl. **8**, 86 (2019).

[33] B. Yao, X. Zang, Z. Li, L. Chen, J. Xie, Y. Zhu, and S. Zhuang, Dual-layered metasurfaces for asymmetric focusing, Photon. Res. **8**, 830 (2020).

[34] P. Georgi, Q. Wei, B. Sain, C. Schlickriede, Y. Wang, L. Huang, and T. Zentgraf, Optical secret sharing with cascaded metasurface holography, Sci. Adv. **7**, eabf9718 (2021).

[35] S. C. Malek, A. C. Overvig, A. Alù, and N. Yu, Multifunctional resonant wavefront-shaping meta-optics based on multilayer and multi-perturbation nonlocal metasurfaces, Light Sci. Appl. **11**, 246 (2022).

[36] B. Wang, F. Dong, Q.-T. Li, D. Yang, C. Sun, J. Chen, Z. Song, L. Xu, W. Chu, Y.-F. Xiao *et al.*, Visible-frequency dielectric metasurfaces for multiwavelength achromatic and highly dispersive holograms, Nano Lett. **16**, 5235 (2016).

[37] Z. Deng, M. Jin, X. Ye, S. Wang, T. Shi, J. Deng, N. Mao, Y. Cao, B. Guan, A. Alù *et al.*, Full-color complex-amplitude vectorial holograms based on multi-freedom metasurfaces, Adv. Funct. Mater. **30**, 1910610 (2020).

[38] S. Du, Z. Liu, C. Sun, W. Zhu, G. Geng, H. Ye, J. Li, and C. Gu, Cross-nanofin-based waveplate pixels for broadband hybrid polarization coding in near-field, Nanophotonics **10**, 1505 (2021).

[39] Y. Cao, L. Tang, J. Li, C. Lee, and Z.-G. Dong, Four-channel display and encryption by near-field reflection on nanoprinting metasurface, Nanophotonics **11**, 3365 (2022).

[40] H. Yuan, Z. Zhong, Y. Zhang, and B. Zhang, Multi-channel image encryption based on an all-dielectric metasurface incorporating near-field nanoprinting and far-field holography, Adv. Opt. Mater. **11**, 2300352 (2023).

[41] J. P. Balthasar Mueller, N. A. Rubin, R. C. Devlin, B. Groever, and F. Capasso, Metasurface polarization optics: Independent phase control of arbitrary orthogonal states of polarization, Phys. Rev. Lett. **118**, 113901 (2017).

[42] Y. Hu, L. Li, Y. Wang, M. Meng, L. Jin, X. Luo, Y. Chen, X. Li, S. Xiao, H. Wang, Y. Luo, C.-W. Qiu, and H. Duan, Trichromatic and tripolarization-channel holography with noninterleaved dielectric metasurface, Nano Lett. **20**, 994 (2019).

[43] Q. Dai, Z. Guan, S. Chang, L. Deng, J. Tao, Z. Li, Z. Li, S. Yu, G. Zheng, and S. Zhang, A single-celled tri-functional metasurface enabled with triple manipulations of light, Adv. Funct. Mater. **30**, 2003990 (2020).

[44] L. Jin, Z. Dong, S. Mei, Y. F. Yu, Z. Wei, Z. Pan, S. D. Rezaei, X. Li, A. I. Kuznetsov, Y. S. Kivshar *et al.*, Noninterleaved metasurface for $(2^6 - 1)$ spin- and wavelength-encoded holograms, Nano Lett. **18**, 8016 (2018).

[45] M. Q. Mehmood, J. Seong, M. A. Naveed, J. Kim, M. Zubair, K. Riaz, Y. Massoud, and J. Rho, Single-cell-driven tri-channel encryption meta-displays, Adv. Sci. **9**, 2203962 (2022).

[46] S. Xiao, T. Wang, T. Liu, C. Zhou, X. Jiang, and J. Zhang, Active metamaterials and metadevices: A review, J. Phys. D: Appl. Phys. **53**, 503002 (2020).

[47] M. Wuttig, H. Bhaskaran, and T. Taubner, Phase-change materials for non-volatile photonic applications, Nat. Photon. **11**, 465 (2017).

[48] F. Ding, Y. Yang, and S. I. Bozhevolnyi, Dynamic metasurfaces using phase-change chalcogenides, Adv. Opt. Mater. **7**, 1801709 (2019).

[49] C. Choi, S. Lee, S. Mun, G. Lee, J. Sung, H. Yun, J. Yang, H. Kim, C. Hwang, and B. Lee, Metasurface with nanostructured $Ge_2Sb_2Te_5$ as a platform for broadband-operating wavefront switch, Adv. Opt. Mater. **7**, 1900171 (2019).

[50] A. Leitis, A. Heßler, S. Wahl, M. Wuttig, T. Taubner, A. Tittl, and H. Altug, All-dielectric programmable Huygens' metasurfaces, Adv. Funct. Mater. **30**, 1910259 (2020).

[51] T. Liu, X. Fang, and S. Xiao, Tuning nonlinear second-harmonic generation in AlGaAs nanoantennas via chalcogenide phase-change material, Phys. Rev. B **104**, 195428 (2021).

[52] S. Abdollahramezani, O. Hemmatyar, M. Taghinejad, H. Taghinejad, A. Krasnok, A. A. Eftekhar, C. Teichrib, S. Deshmukh, M. A. El-Sayed, E. Pop *et al.*, Electrically driven reprogrammable phase-change metasurface reaching 80% efficiency, Nat. Commun. **13**, 1696 (2022).

[53] C. Li, S. Du, R. Pan, X. Xiong, Z. Tang, R. Zheng, Y. Liu, G. Geng, J. Sun, C. Gu, H. Guo, and J. Li, Phase change materials-based bilayer metasurfaces for near-infrared photonic routing, Adv. Funct. Mater. 2310626 (2023).

[54] M. Delaney, I. Zeimpekis, D. Lawson, D. W. Hewak, and O. L. Muskens, A new family of ultralow loss reversible phase-change materials for photonic integrated circuits: Sb_2S_3 and Sb_2Se_3, Adv. Funct. Mater. **30**, 2002447 (2020).

[55] L. Lu, Z. Dong, F. Tijiptoharsono, R. J. H. Ng, H. Wang, S. D. Rezaei, Y. Wang, H. S. Leong, P. C. Lim, J. K. W. Yang, and R. E. Simpson, Reversible tuning of Mie resonances in the visible spectrum, ACS Nano **15**, 19722 (2021).

[56] S. Luo, Z. Zhang, X. He, Z. Zhang, X. Li, M. Fu, and J. Yang, Design of reflective tunable structural color metasurface based on guided-mode resonance filter and Sb_2S_3, Photonics **10**, 752 (2023).

[57] K. Liu, Z. Lin, B. Han, M. Hong, and T. Cao, Non-volatile dynamically switchable color display via chalcogenide stepwise cavity resonators, Opto-Electron. Adv. **7**, 230033 (2024).

[58] S. Qin, N. Xu, H. Huang, K. Jie, H. Liu, J. Guo, H. Meng, F. Wang, X. Yang, and Z. Wei, Near-infrared thermally modulated varifocal metalens based on the phase change material Sb_2S_3, Opt. Express **29**, 7925 (2021).

[59] L. Chen, Y. Hao, L. Zhao, R. Wu, Y. Liu, Z. Wei, N. Xu, Z. Li, and H. Liu, Multifunctional metalens generation using bilayer all-dielectric metasurfaces, Opt. Express **29**, 9332 (2021).

[60] P. Moitra, Y. Wang, X. Liang, L. Lu, A. Poh, T. W. Mass, R. E. Simpson, A. I. Kuznetsov, and R. Paniagua-Dominguez, Programmable wavefront control in the visible spectrum using low-loss chalcogenide phase-change metasurfaces, Adv. Mater. **35**, 2205367 (2022).

[61] T. Liu, Z. Han, J. Duan, and S. Xiao, Phase-change metasurfaces for dynamic image display and information encryption, Phys. Rev. Appl. **18**, 044078 (2022).

[62] T. Liu, D. Zhang, W. Liu, T. Yu, F. Wu, S. Xiao, L. Huang, and A. E. Miroshnichenko, Phase-change nonlocal metasurfaces for dynamic wave-front manipulation, Phys. Rev. Applied **21**, 044004 (2024).

[63] W. Dong, H. Liu, J. K. Behera, L. Lu, R. J. H. Ng, K. V. Sreekanth, X. Zhou, J. K. W. Yang, and R. E. Simpson, Wide bandgap phase change material tuned visible photonics, Adv. Funct. Mater. **29**, 1806181 (2018).

[64] Z. Fang, J. Zheng, A. Saxena, J. Whitehead, Y. Chen, and A. Majumdar, Non-volatile reconfigurable integrated photonics enabled by broadband low-loss phase change material, Adv. Opt. Mater. **9**, 202002049 (2021).

[65] O. Hemmatyar, S. Abdollahramezani, I. Zeimpekis, S. Lepeshov, A. Krasnok, A. I. Khan, K. M. Neilson, C. Teichrib, T. Brown, E. Pop *et al.*, Enhanced meta-displays using advanced phase-change materials, arXiv:2107.12159.

[66] K. Gao, K. Du, S. Tian, H. Wang, L. Zhang, Y. Guo, B. Luo, W. Zhang, and T. Mei, Intermediate phase-change states with improved cycling durability of Sb_2S_3 by femtosecond multi-pulse laser irradiation, Adv. Funct. Mater. **31**, 2103327 (2021).